Chinese Chemical Letters 36 (2025) 109650

Contents lists available at ScienceDirect

Chinese Chemical Letters

journal homepage: www.elsevier.com/locate/cclet

Unraveling the reaction mechanism of high reversible capacity CuP_2/C anode with native oxidation PO_x component for sodium-ion batteries

Huixin Chen[a,b,f], Chen Zhao[b,f], Hongjun Yue[b,f,*], Guiming Zhong[b,d,f], Xiang Han[c,*], Liang Yin[e], Ding Chen[a,*]

[a] State Key Laboratory of Advanced Design and Manufacturing for Vehicle Body, College of Mechanical and Vehicle Engineering, Hunan University, Changsha 410082, China
[b] CAS key Laboratory of Design and Assembly of Functional Nanostructures, and Fujian Provincial Key Laboratory of Nanomaterials, Fujian Institute of Research on the Structure of Matter, Chinese Academy of Sciences, Fuzhou 350002, China
[c] College of Materials Science and Engineering, Co-Innovation Center of Efficient Processing and Utilization of Forest Resources, Nanjing Forestry University, Nanjing 210037, China
[d] Laboratory of Advanced Spectro-electrochemistry and Li-ion Batteries, Dalian Institute of Chemical Physics, Chinese Academy of Sciences, Dalian 116023, China
[e] Institute of Physics, Chinese Academy of Sciences, Beijing 100190, China
[f] Xiamen Key Laboratory of Rare Earth Photoelectric Functional Materials, Xiamen Institute of Rare Earth Materials, Haixi institutes, Chinese Academy of Sciences, Xiamen 361021, China

ARTICLE INFO

Article history:
Received 21 January 2024
Accepted 7 February 2024
Available online 10 February 2024

Keywords:
CuP_2/C composite
POx component
Reaction mechanism
Solid-state NMR
Sodium-ion batteries

ABSTRACT

Phosphorus-based anode is a promising anode for sodium-ion batteries (SIBs) due to its high specific capacity, however, suffers from poor electronic conductivity and unfavorable electrochemical reversibility. Incorporating metals such as copper (Cu) into phosphorus has been demonstrated to not only improve the electronic conductivity but also accommodate the volume change during cycling, yet the underline sodiation mechanism is not clear. Herein, take a copper phosphide and reduced graphene oxide (CuP_2/C) composite as an example, which delivers a high reversible capacity of >900 mAh/g. Interestingly, it is revealed that the native oxidation PO_x components of the CuP_2/C composite show higher electrochemical reversibility than the bulk CuP_2, based on a quantitative analysis of high-resolution solid-state ^{31}P NMR, *ex-situ* XPS and synchrotron X-ray diffraction characterization techniques. The sodiation products Na_3PO_4 and $Na_4P_2O_7$ derived from PO_x could react with Na-P alloys and regenerate to PO_x during charge process, which probably accounts for the high reversible capacity of the CuP_2/C anode. The findings also illustrate that the phosphorus transforms into nanocrystalline Na_3P and Na_xP alloys, which laterally shows crystallization-amorphization evolution process during cycling.

In the past decade, lithium-ion batteries (LIBs) have been widely applied in portable electronics, electrical vehicles and other energy storage devices. To meet the demands with further increasement of low-cost and large-scale energy storage devices, sodium ion batteries (SIBs) or sodium-sulfur (Na-S) batteries are considered as promising candidate because of its abundant reserves and even distribution of sodium resource in earth crust [1–3]. Compared with Cu foil as anode current collectors for LIBs, Al foil that applied in SIBs is cost effectiveness. Although the fundamental mechanism is almost the same with LIBs, the molar mass of Na is heavier that is 23.00 compared to 6.94 (Li) and the atomic diameter is larger that is 1.02 Å regarded to 0.76 Å (Li-ion), which not only sacrifices in gravimetric and energy density of SIBs but also induces different sodium mechanism, such as complex electrochemical reactions and relatively low reaction kinetics [4,5].

To develop high-energy SIBs, it is significant to design high-capacity and appropriate-redox-potential electrode materials. However, suitable high-performance anode materials for SIBs are still challenging [6,7]. Recently, red phosphorus (rP) as anode has been paid much attention to because of its highest theoretical capacity of 2596 mAh/g (in view of reaction of P with three Na^+ to form Na_3P) [8,9]. But its low intrinsic electronic conductivity and large volume swelling during cycling are to the disadvantage of application [10]. Introducing metal to phosphors to form metal phosphides (MP_x) is a proven method to mitigate the issues, for example Cu, Sn, and Ge [11–13]. Carbon coating, such as hard carbon,

* Corresponding authors.
E-mail addresses: hjyue@fjirsm.ac.cn (H. Yue), hanxiang@njfu.edu.cn (X. Han), chending@hnu.edu.cn (D. Chen).

https://doi.org/10.1016/j.cclet.2024.109650
1001-8417/

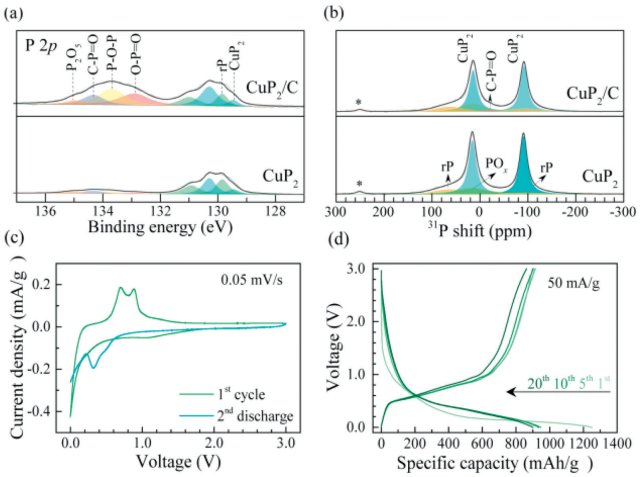

Fig. 1. The physical characterization of as-synthesized CuP_2 and CuP_2/C materials: (a) XPS P 2p spectra and (b) solid-state ^{31}P NMR spectra. The asterisks indicate the spinning sidebands. The electrochemical profiles of CuP_2/C material as anode for SIBs: (c) CV curves at a scan rate of 0.05 mV/s and (d) electrochemical profiles during cycling at 50 mA/g. The specific capacity and applied current densities are based on the mass of CuP_2 material exclusive of carbon.

multilayer graphene (mG) and carbon nanotubes were also widely applied to enhance the conductivity and release the mechanical stress during cycling [14–17]. Additionally, the discharge product of MP_x-Na_3P has been investigated by X-ray diffraction (XRD), high resolution transmission electron microscopy (HRTEM) and selected area electron diffraction (SAED) [18–22]. The deficiencies of above conventional diffraction measurements are difficult to obtain information about amorphous phase, thus the electrochemical sodium storage mechanisms during (dis)charging are not fully understood.

In this work, a copper phosphide and reduced graphene oxide (CuP_2/C) composite material was synthesized by a simple ball milling method, which show a high reversible specific capacity of >900 mAh/g. Taking this composite anode as a sample, the sodiation and desodiation mechanism and quantitative phase transformation CuP_2/C were explored and revealed by the techniques of synchrotron XRD, *ex-situ* XPS and solid-state NMR. For the first time, it is found that the native PO_x on the surface of CuP_2/C composite show higher electrochemical reversibility than the bulk CuP_2, due to the existence of Cu catalyst. The PO_x firstly sodiates and forms Na_3PO_4 and $Na_4P_2O_7$ during the first discharge process, after that the above sodiation products react with Na-P alloys and recover to PO_x during charge process. The reversible phase transformation of PO_x accounts for the high reversible capacity of the CuP_2/C composite anode. The findings also illustrate that the phosphorus transforms into nanocrystalline NaP, Na_3P and Na_xP alloys, among which the size of nanocrystals becomes smaller along cycling and shows crystallization-amorphization evolution process during long-life test. Our work sheds light on the material design of phosphorus-based anode with high capacity and electrochemical reversibility toward high energy density SIBs.

The synthesis details of CuP_2/C are provided in Experimental Section in Supporting information. For simplicity, CuP_2/C is firstly taken as an example for illustration. Fig. S1a (Supporting information) shows the XRD patterns of CuP_2 and CuP_2/C materials, all peaks can be assigned to CuP_2 phase (JCPDS No. 076–1190) with a monoclinic lattice structure [23]. Compared with CuP_2, the CuP_2/C composite exhibits almost the same diffraction peaks, implying the ball milling process does not change the crystalline nature of CuP_2. To investigate the chemical composition and bonding state of above materials, XPS was carried out. In P 2p spectra in Fig. 1a, there is a broad peak at around 130 eV for both samples, which is matched with the CuP_2 and pristine rP. Additionally, broad peaks appear at 132.9, 133.7 and 135.0 eV due to the surface oxidation of rP, the first two peaks indicate the formation of P−O−P and O−P=O bonds [24], and the last one belongs to P_2O_5. The P_2O_5 was obtained during the ball milling process, which is inevitably incorporating some extent of air. At the same time, the size becomes smaller and the surface area increase, as a result, the reactivity between P and O increases and forms some native P_2O_5 on the surface. The peak at 134.3 eV corresponds to C−P=O bond, in which the C element is probably due to the inevitable C-containing contaminants in CuP_2. Conspicuously, above four peaks all intensified in the CuP_2/C composite. The XPS Cu 2p spectra in Fig. S1b (Supporting information) shows the two characteristic peaks, which are associated with Cu(I) $2p_{3/2}$ (932.9 eV) and $2p_{1/2}$ (952.7 eV), respectively [25]. Solid-state ^{31}P NMR spectra in Fig. 1b were collected to present a quantitative understanding about the materials. Two intense peaks located at 15 and −91 ppm is observed for both samples, corresponding to two P sites in the crystal structure of CuP_2 as illustrated in Fig. S2 (Supporting information). Another two broad resonances at ~62.7 and −95.2 ppm is ascribed to the unreacted rP. A broad peak located at ~15 ppm attributed to the P−O bonding is distinguished. A weak peak at ~−20 ppm detected in CuP_2/C composite is assigned to the C−P=O bond, which is produced during the ball-milling process by the reaction of reduced graphene oxide and PO_x. The morphologies of CuP_2 and CuP_2/C materials are characterized by SEM and TEM. In Fig. S1c (Supporting information), CuP_2 is composed of irregular shape of particles in a range of 300−600 nm. While for CuP_2/C composite in Fig. S1d (Supporting information), smaller particles with a diameter of 100−300 nm observed, which should be generated during ball milling process. High resolution TEM (HRTEM) image in Fig. S1e (Supporting information) manifests that CuP_2/C composite has a crystal core with amorphous carbon shell. The marked parallel fringes have the space of ~0.289 nm, corresponding to the $(\bar{1}12)$ plane of CuP_2, which is in good agreement with the XRD patterns. Such a carbon layer will enhance the electronic conductivity and accommodate the volume variation during (dis)charge.

The electrochemical profiles were firstly evaluated by CV between 0 and 3 V at 0.05 mV/s *versus* Na^+/Na and presented in Fig. 1c. During the initial cathodic sweep, there is a broad wave ranging from 1.6 V to 0.7 V, which is indicative of the decomposition of electrolyte and the formation of SEI (solid electrolyte interphase) layer on the fresh electrode. Upon further sodiation to 0 V, the current density increases continuously, stating that the occurrence of electrochemical sodiation on CuP_2/C electrode. In the ensuing anodic sweep, two pronounced peaks centered at 0.70 and 0.89 V correspond to multi-step desodiation process from NaP and Na_3P to P. By contrast, in the second discharge process, a peak located at 0.32 V appears contributed to the sodiation of amorphous rP, and the broad wave (1.6−0.7 V) disappears due to the absence of SEI contribution, which is different from the first cycle. The specific capacity is calculated based on the total mass of CuP_2, PO_x and carbon, the mass loading is about 2 mg/cm^2 on each of the discs for performance tests and 4 mg/cm^2 for synchrotron XRD, *ex-situ* NMR characterization, respectively. Fig. 1d shows the voltage profiles of CuP_2/C electrode at a current density of 50 mA/g, the specific capacity of the initial discharge can reach up to 1200 mAh/g (normalized to the mass of CuP_2 exclusive of carbon), and roughly 900 mAh/g is recovered when the electrode is fully charged. Notably, the reversible capacity of ~900 mAh/g is lower than the theoretical value of 1281 mAh/g according to the formation of Na_3P, which has been reported in the P-based sodium storage materials [26–31]. The rate performance and high rate cycling were also tested. As shown in Fig. S3 (Supporting information), the specific capacities of CuP_2/C at 0.05, 0.2, 0.5, 1, and 2 A/g are 950, 880, 815, 708 and 595 mAh/g, respectively. Even at a high rate of

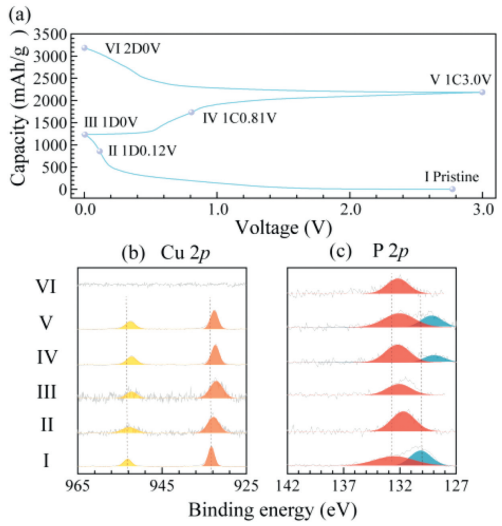

Fig. 2. (a) The electrochemical profiles of CuP_2/C electrodes for SIBs at 25 mA/g. (b) XPS Cu 2p spectra and (c) XPS P 2p spectra.

1 A/g, the CuP_2/C anode could deliver a reversible capacity of 550 mAh/g after 50 cycles (Fig. S4 in Supporting information). With the purpose of elucidating the underlying sodiation/desodiation mechanism of CuP_2/C composite, we disassemble the coin cells at certain (dis)charged states and track the phase evolution by *ex-situ* studies.

To investigate the reaction mechanism of CuP_2/C composite as anode for SIBs, the crystal structure variation during (dis)charge process is researched by synchrotron XRD (Fig. S5 in Supporting information). The pattern of each state shows no pronounced peaks ascribed to other crystal phases as (dis)charge proceeds, indicating that amorphous phases present in addition to the residual CuP_2 material.

The surface oxidation states of the CuP_2/C electrode at selected voltage points during cycling, as shown in Fig. 2a, were investigated by *ex-situ* XPS. Fig. 2b displays the XPS spectra of Cu 2p at (dis)charged states: the pristine electrode featuring Cu(I) $2p_{1/2}$ (953.1 eV) and Cu $2p_{3/2}$ (933.2 eV) [25]. As discharge goes on, the peaks of Cu 2p all move to lower E_b. When fully charged to 3 V (VI), all of peaks shifted in the higher E_b direction, implying the occurrence of reversible electrochemical reaction. And at 2D0V (discharged to 0 V in the second discharge process, similarly hereinafter) state, it is distinct that no peaks of Cu(I) are observed compared with 1D0V state, indicating possibly that the influence of high S/N (signal/noise) ratio. In Fig. 2c, the P 2p spectra at different voltages display a peak centered at ~132 eV, which is attributed to the sodium phosphorus intermediates, Na_xP ($x = 1$–3) [32]. The peak at ~130 eV is corresponding to the rP and CuP_2, which is consistent with the result in Fig. 1a.

In addition, Cu-K edge XAS analysis was employed to further resolve the structural ambiguities of above weak XRD patterns and to probe the structural variations around Cu ions during electrochemical process of the CuP_2/C electrode. In the X-ray absorption near-edge structure (XANES) region (Fig. S6a in Supporting information), the pristine electrode exhibited a Cu^I-like characteristic feature with a peak located at ~8986 eV assigned to a single bond of $1s \rightarrow 4p\pi^*$, the intensity of which suggests the four-fold coordination geometry of the Cu site. This hypothesis is evidenced by the structure presentation of CuP_2 as illustrated in Fig. S2. For Cu^I, the transition shows highest intensity for the linear two-coordinated complexes and becomes less intense and broaden as the coordination number increases [33]. This peak gradually becomes weak with an increase of the depth of discharge. Upon subsequent charge, the XANES feature returned incompletely to its initial state. The second discharge process is similar with the first one. More interestingly, the radial distribution functions of the Fourier-transformed (FT) k^2-weight extended X-ray absorption fine structure (EXAFS) spectra (Fig. S6b in Supporting information) present a distinct geometric structure variation around the central Cu ion. Yet surprisingly, an apparent peak at ~2 Å corresponding to the Cu-O shell is viewed. Upon discharge, this peak shifts to the higher **r** space region, indicating a distinct elongating of the bond length of the CuP_2/C electrode. During the consecutive charge process, the structure is reversibly recovered. *Ex-situ* XRD was performed to further confirmed the crystalline phase transformation of CuP_2/C electrode for the first cycle and second discharge processes (Fig. S7 in Supporting information). In Fig. S5a, the diffraction intensity of crystalline CuP_2 decrease during the discharge process, implying the CuP_2 transforms into sodiation products. Even after recharged to 3 V, no obvious diffraction peak was observed, demonstrating the CuP_2 becomes amorphous after initial cycle. Expectedly, no crystalline peak was detected during the second discharge process (Fig. S5b). The *ex-situ* XRD results further confirms the phase transformation of CuP_2 during charge and discharge. The crystalline phase transformation of CuP_2/C during cycling was revealed while the amorphous phases needed to be further explored.

To elucidate the structural evolution including crystal and amorphous states of the CuP_2/C composite during cycling, the usage of solid-state ^{31}P NMR (Fig. 3) was conducive to circumvent the disadvantage of the traditional diffraction method, and quantify the variation of amorphous products. Accordingly, the peaks at −91 and 15 ppm are ascribed to CuP_2 phase, the areal ratio of which is around 1:1. The peaks at 14.1 and 2.5 ppm are Na_3PO_4 and $Na_4P_2O_7$, respectively [34,35]. In this case, with the Cu catalyst, the PO_x on the surface tends to be electrochemical active and transforms into Na-P-O at the early stage of the sodiation process, such as 1D0.65 V. With the sodiation process continues, the Na-P-O reacts with more Na atoms and forms Na_3PO_4 and other being $Na_4P_2O_7$ products, as a result, the peak the transition state of phosphates is divided into two peaks. Red phosphorus shows two relatively broad peaks with FWHM of ~100 ppm, which are located at −95.2 and 62.7 ppm [36]. The presence of two environments of associated ^{31}P shifts at −29 and −78 ppm that are correspond to amorphous NaP. While for Na_3P, there are four environments of shifts at −118, −180, −238 and −280 ppm. Thereinto, the peak of −238 ppm with width of 10 ppm is probably originated in the Na_xP species formed in side reactions, minor Na_xP intermediates, or Na near P defects (such as the end of a P chain) [37]. Based on above discussion, we can analysis each *ex-situ* state during cycling.

Solid-state ^{31}P NMR spectra were further collected to gain a quantitative understanding on the prepared materials. The content of PO_x on the surface was determined by NMR fitting analysis. Two intense ^{31}P NMR peaks located at 15 and −91 ppm, corresponding to two P sites in CuP_2. Two other broad resonances at 62.7 and −95.2 ppm which are due to the unreacted rP as shown in the fitting plots. And a broad peak located at ~15 ppm is distinguished and attributed to the P–O bonding. It is noted that the fitting analysis indicates that the atomic ratio of P in CuP_2, rP and P–O bonds (PO_x) is around 7:1.5:1.5. Also, the contents keep dropping as discharge proceeds on. Additionally, the peak of C−P=O bond shows the shift at −21 ppm with a width of 25 ppm, which is located at the same position of PO_x. During the first discharge, when the voltage is downs to 0.65 V (1D0.65 V, discharged to 0.65 V in the first discharge process, similarly hereafter), there is a peak with FWHM of ~20 ppm at 2.9 ppm accompanied with the vanishment of C−P=O bond, which is attributed to the transition state of phosphates. Then in the state of 1D0.26 V, the peak of mentioned transition state is divided into two peaks. One is the peak at 14.1 ppm

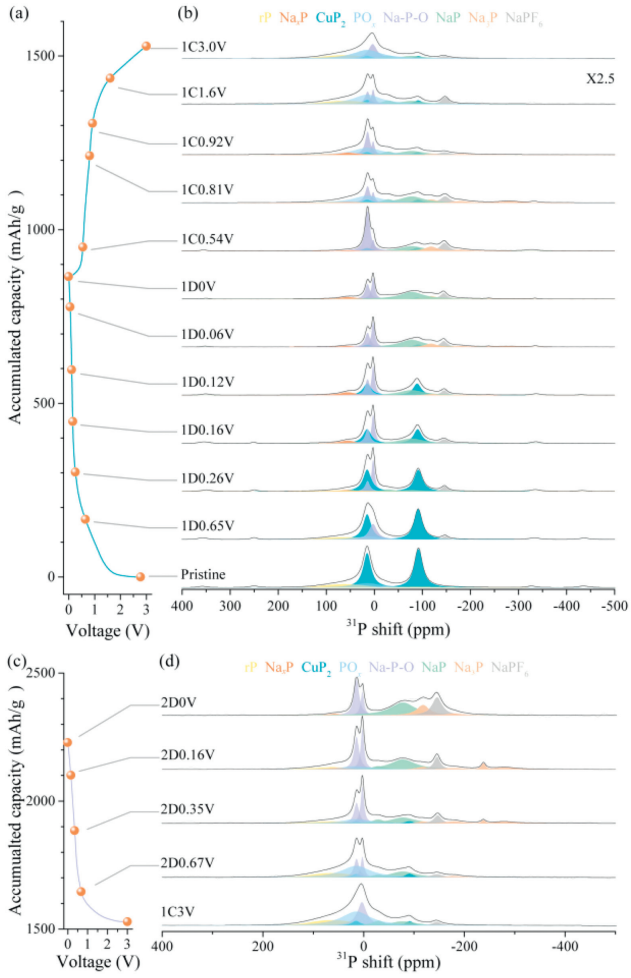

Fig. 3. Tracking the structural evolution of CuP_2/C electrodes for SIBs in the first cycle by solid-state ^{31}P NMR spectroscopy: (a) The electrochemical profiles of the CuP_2/C electrode at a current of 25 mA/g. (b) Solid-state ^{31}P NMR spectra of the CuP_2/C electrodes at selected states. Tracking the structural evolution of CuP_2/C electrodes for SIBs in the second discharge process by solid-state ^{31}P NMR spectroscopy: (c) The electrochemical profiles of the CuP_2/C electrode at a current of 25 mA/g. (d) Solid-state ^{31}P NMR spectra of the CuP_2/C electrodes at selected states.

with width of 12 ppm of Na_3PO_4, the other is the peak at 2.5 ppm with width of 8 ppm of $Na_4P_2O_7$. It is worth mentioning that the content of Na_3PO_4 gradually increases but that of $Na_4P_2O_7$ is almost unchanged. Meanwhile, the phases of Na_xP and amorphous NaP (*a*-NaP) are observed along with the disappearance of PO_x. The peak of Na_xP centers at 55 ppm with width of 40 ppm. In the next state (1D0.16 V), rP vanishes. When the voltage discharged to 0.12 V (1D0.12 V), the phase of Na_3P generates, three of which could be viewed (shifts at −118, −180, −238 ppm with FWHM of 30, 40, 10 ppm, respectively). Above the contents of *a*-NaP and Na_3P all increase with discharged depth raising. For 1D0.06 V, fourth peak of Na_3P appears at −280 ppm with width of 50 ppm. In short, the discharge process is linked to a conversion of CuP_2, rP and PO_x to Na-P alloys and phosphates. To demonstrate the role of Cu on the electrochemical reversibility of rP, the NMR data of P/C during charge and discharge was carried out. As shown in Fig. S8 (Supporting informatio), the PO_x peak remains almost the same during initial discharge and charge processes, indiacating that the PO_x is electrochemical inactive, which is totally different with the CuP_2 results. Based on the above results, it is concluded that, the native oxide PO_x on the surface of CuP_2/C becomes electrochemical active and reversible under the existence of Cu catalyst.

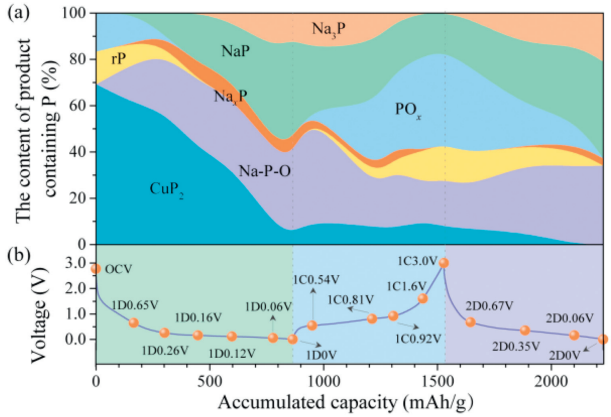

Fig. 4. Phase transformation diagram for the CuP_2/C composite with the galvanostatic (dis)charge processes: (a) The contents of produced Na-P alloys and Na-P-O compounds can be directly read in the Y axis, depending on the deconvolution results of *ex-situ* ^{31}P NMR spectra in Fig. 3. (b) The electrochemical profiles of the CuP_2/C electrode cycling at a current of 25 mA/g.

To better understand the sodiation/desodiation mechanism of CuP_2/C, based on the ^{31}P NMR spectra during the galvanostatic (dis)charge processes, the quantitative phase transformation diagram is analyzed (detailed in Table S1 in Supporting information) and shown in Fig. 4. Generally speaking, the diagram exhibits the reversibility of CuP_2, rP and PO_x, especially for the high electrochemical reversibility of PO_x. After the first desodiation, only a small ratio of CuP_2 convert to the initial state but PO_x shows high reversibility. It should be noted that the content of PO_x is higher than the pristine CuP_2/C before cycling, which may be caused by atomic structure reconstruction between P and O atoms during cycling. Instead, the Na-O-P and Na-P alloy derived from CuP_2 convert to PO_x, rP and CuP_2, which should be the main reason responsible for the high reversibility of the unique CuP_2/C anode. Besides, after the initial desodiation process, the residual Na-P alloy such as Na_xP, Na_3PO_4 and $Na_4P_2O_7$ may contribute to the irreversible capacity loss and low Coulombic efficiency. It is suggested that the mechanical stress caused by volume expansion could be regulated by controlling the content of PO_x in the phosphorus-based anodes. In addition, reducing the content of Na_xP, Na_3PO_4 and $Na_4P_2O_7$ is expected to improve the reversibility and Coulombic efficiency. For the second cycle, the contents of NaP and Na_3P alloy increased compared to the initial cycle, which may be induced by the particles fracture and converting into nanosized P, thus enabling fast sodiation kinetics. During the sodiation process of rP, Na_xP and NaP forms at the same time with the disappearance of PO_x. With the sodiation continues, more Na atoms insert into and forms more NaP and Na_xP. At the end of sodiation process, some extent of Na_xP trnaforms into Na_3P. The NaP and Na_3P tend to be amorphous and degree of disorder increase along repeated cycles.

In summary, combination of synchrotron XRD, *ex-situ* XPS and NMR, it is revealed that native oxidation components such as PO_x of the CuP_2/C composite show better electrochemical reversibility even than the bulk CuP_2. The surface PO_x firstly sodiate and generate Na_3PO_4 and $Na_4P_2O_7$ during charge process, and substantially react with Na-P alloys and recover to the PO_x during the desodiation process. This is a critical factor that accounts for the high reversible capacity of 900 mAh/g for the CuP_2/C composite. It is also demonstrated that the formation of amorphous Na_3P and Na_xP along repeated cycles. This work for the first time provides a quantitative understanding on the electrochemical sodiation mechanism of the CuP_2/C composite, which shed light on a new road to design high-capacity P-based anode materials for sodium storage by manipulating the content and bonding nature between P and oxygen.

Declaration of competing interest

The authors declare that they have no known competing financial interests or personal relationships that could have appeared to influence the work reported in this paper.

Acknowledgements

This work was financially supported by National Nature Science Foundation of China (Nos. 21805278, 22272175 and 22209075), the Fujian Science and Technology Planning Projects of China (Nos. 2022T3067 and 2023H0045), the Self-deployment Project Research Programs of Haixi Institutes, Chinese Academy of Sciences (No. CXZX-2022-JQ12), the Self-deployment project of XIREM (No. 2023GG02).

Supplementary materials

Supplementary material associated with this article can be found, in the online version, at doi:10.1016/j.cclet.2024.109650.

References

[1] N.T. Aristote, K. Zou, A. Di, et al., Chin. Chem. Lett. 33 (2022) 730–742.
[2] C. Ma, X. Wang, J. Lan, et al., Adv. Funct. Mater. 33 (2022) 2211821.
[3] J. He, A. Bhargav, L. Su, et al., Nat. Commun. 14 (2023) 6568.
[4] Na-Ion batteries K. Kubota, S. Komaba, S. Passerini, D. Bresser, A. Moretti, A. Varzi, Encyclopedia of Electrochemistry Wiley-VCH Verlag GmbH & Co KGaA, Weinheim, 2020, pp. 1–64.
[5] N. Yabuuchi, K. Kubota, M. Dahbi, et al., Chem. Rev. 114 (2014) 11636–11682.
[6] H. Wang, H. Chen, C. Chen, et al., Chin. Chem. Lett. 34 (2023) 107465.
[7] B. Qin, M. Wang, S. Wu, et al., Chin. Chem. Lett. 35 (2024) 108921.
[8] H. Tan, D. Chen, X. Rui, et al., Adv. Funct. Mater. 29 (2019) 1808745.
[9] J. Ge, C. Ma, Y. Wan, et al., Adv. Funct. Mater. 33 (2023) 2305803.
[10] F.H. Yang, H. Gao, J. Chen, et al., Small Methods 1 (2017) 1700216.
[11] S.O. Kim, A. Manthiram, ACS Appl. Mater. Interfaces 9 (2017) 16221–16227.
[12] Y. Kim, Y. Kim, A. Choi, et al., Adv. Mater. 26 (2014) 4139–4144.
[13] W. Li, X. Li, J. Liao, et al., Energy Storage Mater. 20 (2019) 380–387.
[14] Y. Kim, Y. Park, A. Choi, et al., Adv. Mater. 25 (2013) 3045–3049.
[15] J. Qian, X. Wu, Y. Cao, et al., Angew. Chem. Int. Ed. 52 (2013) 4633–4636.
[16] J. Sun, H.W. Lee, M. Pasta, et al., Nat. Nanotechnol. 10 (2015) 980–985.
[17] W.J. Li, S.L. Chou, J.Z. Wang, et al., Nano Lett. 13 (2013) 5480–5484.
[18] Q. Liu, Z. Hu, Y. Liang, et al., Angew. Chem. Int. Ed. 59 (2020) 5159–5164.
[19] Y. Lu, P. Zhou, K. Lei, et al., Adv. Energy Mater. 7 (2017) 1601973.
[20] L. Ran, B. Luo, I.R. Gentle, et al., ACS Nano 14 (2020) 8826–8837.
[21] T. Wang, K. Zhang, M. Park, et al., ACS Nano 14 (2020) 4352–4365.
[22] X. Wang, K. Chen, G. Wang, et al., ACS Nano 11 (2017) 11602–11616.
[23] C. Zhao, H. Chen, H. Liu, et al., J. Mater. Chem. A 9 (2021) 6274–6283.
[24] P. Nakhanivej, X. Yu, S.K. Park, et al., Nat. Mater. 18 (2019) 156–162.
[25] A.Y. Kim, M.K. Kim, K. Cho, et al., ACS Appl. Mater. Interfaces 8 (2016) 19514–19523.
[26] Q. Li, Z. Li, Z. Zhang, et al., Adv. Energy Mater. 6 (2016) 1600376.
[27] F.P. Zhao, N. Han, W.J. Huang, et al., J. Mater. Chem. A 3 (2015) 21754–21759.
[28] S. Kaushik, J. Hwang, K. Matsumoto, et al., ChemElectroChem 5 (2018) 1340–1344.
[29] S.O. Kim, A. Manthiram, Chem. Commun. 52 (2016) 4337–4340.
[30] S. Chen, F. Wu, L. Shen, et al., ACS Nano 12 (2018) 7018–7027.
[31] Y. Zhang, G. Wang, L. Wang, et al., Nano Lett. 19 (2019) 2575–2582.
[32] Y. Yan, S. Xia, H. Sun, et al., Chem. Eng. J. 393 (2020) 124788.
[33] I.J. Pickering, G.N. George, C.T. Dameron, et al., J. Am. Chem. Soc. 115 (1993) 9498–9505.
[34] S. Hayashi, K. Hayamizu, B. Chem. Soc. Jap. 62 (1989) 3061–3068.
[35] S. Hayashi, K. Hayamizu, Chem. Phys. Lett. 161 (1989) 158–162.
[36] C. Marino, M. El Kazzi, E.J. Berg, et al., Chem. Mater. 29 (2017) 7151–7158.
[37] L.E. Marbella, M.L. Evans, M.F. Groh, et al., J. Am. Chem. Soc. 140 (2018) 7994–8004.